

# R-AGNO-RPN: A LIDAR-Camera Region Proposal Deep Network for Resolution-Agnostic Object Detection

Ruddy Théodose<sup>1,2</sup>, Dieumet Denis<sup>1</sup>, Thierry Chateau<sup>2</sup>, Vincent Frémont<sup>3</sup> and Paul Checchin<sup>2</sup>

**Abstract**—Current neural networks-based object detection approaches processing LiDAR point clouds are generally trained from one kind of LiDAR sensors. However, their performances decrease when they are tested with data coming from a different LiDAR sensor than the one used for training, i.e., with a different point cloud resolution. In this paper, R-AGNO-RPN, a region proposal network built on fusion of 3D point clouds and RGB images is proposed for 3D object detection regardless of point cloud resolution. As our approach is designed to be also applied on low point cloud resolutions, the proposed method focuses on object localization instead of estimating refined boxes on reduced data. The resilience to low-resolution point cloud is obtained through image features accurately mapped to Bird’s Eye View and a specific data augmentation procedure that improves the contribution of the RGB images. To show the proposed network’s ability to deal with different point clouds resolutions, experiments are conducted on both data coming from the KITTI 3D Object Detection and the nuScenes datasets. In addition, to assess its performances, our method is compared to PointPillars, a well-known 3D detection network. Experimental results show that even on point cloud data reduced by 80% of its original points, our method is still able to deliver relevant proposals localization.

**Index Terms**—Deep Learning, 3D Object Detection, Sensor Fusion, Intelligent Vehicle, Camera Sensor, LiDAR Sensor.



## 1 INTRODUCTION

Autonomous driving in urban scenes remains nowadays a tremendous challenge. The autonomous vehicle must simultaneously manage multiple aspects of perception such as scene analysis, traffic sign recognition or moving object localization before deciding which action must be engaged to preserve the safety of the other users and its own safety too. 3D object detection for autonomous vehicles is an active research topic since identifying the parts of the scene that can interfere with the vehicle trajectory, is a crucial task within the navigation pipeline. In this field, most advances rely essentially on LiDAR sensors data.

Indeed, LiDAR sensors deliver 3D point cloud depicting the surroundings of the sensor with high accuracy. However, the 3D point clouds are not delivered in a unique and normalized data structure, and the spatial positioning of points is irregular. Moreover, little information on the surfaces’ appearance is provided. By contrast, cameras deliver dense and structured data depending on which part of the spectrum is captured (color information, infrared, etc.). These features make them particularly adapted for classification or identification tasks, even on small or noisy images. However, the loss of the depth information due to the projection process and their narrow field of view, makes difficult the full 3D reconstruction of the scene geometry. Over the past years, deep neural networks have proven their efficiency in perception tasks by using camera images. Most methods aim to extend these

techniques to 3D point clouds. However, due to the data type differences between images and 3D LiDAR information, the 3D point cloud data structure for neural networks is still an open problem. Some methods for example transform their sparse data into dense and structured grids through voxelization that can then use operators initially designed for image processing [1]. Other works exploit architectures based on PointNet [2], [3] with the aim to directly process the 3D point cloud by exploiting the geometric relationships between points and their neighborhood [4], [5].

In the field of Autonomous Vehicles, most of them are equipped with at least these two types of sensors in order to benefit their respective assets while counterbalancing the disadvantages of each one. However, few methods employ the data fusion of the two sensors due to their different data structure format and the constraints that have to be defined between the two sensors (required calibration, two pieces of data to process, 3D and image space to manage, etc.). Currently, the majority of 3D object detection methods are purely LiDAR-based. However, some methods exploit the outputs of 2D processing techniques to constraint the locations of the possible locations. For example, the use of image semantic segmentation [6] or 3D frustums generated by 2D image detection [7] are useful priors for the 3D detection task.

While advances focused on the design of architectures that allow to maximize accuracy, most of the existing models are trained from a given set of LiDAR parameters and do not generalize well if tested on another set. If solutions have been developed for camera sensors (like domain adaptation [8]), to the best of our knowledge, almost no work has analyzed the effects of 3D point clouds issued from different LiDAR sensors on pre-trained systems. Therefore, we believe that this topic is a major stake, as the acquisition and annotation data process for 3D detection is expensive and time-consuming. Moreover, the reuse of a pre-

<sup>1</sup> *Sherpa Engineering, R&D Department, 333 Avenue Georges Clemenceau, 92000 Nanterre, France.* [r.theodose, d.denis]@sherpa-eng.com

<sup>2</sup> *Université Clermont Auvergne, CNRS, SIGMA Clermont, Institut Pascal, F-63000 Clermont-Ferrand, France.* firstName.lastName@uca.fr

<sup>3</sup> *Centrale Nantes, LS2N, UMR CNRS 6004, Nantes, France.* vincent.fremont@ls2n.fr

trained deep network that is agnostic to the installed 3D LiDAR, might bring a potential boost in the annotation process.

In this paper, we propose a new Region Proposal Network (RPN) using 3D LiDAR data and camera images that is independent regarding the 3D point cloud resolution as illustrated in Figure 1. Our RPN first takes as input a color image and returns a first feature map that is sampled on places defined by the LiDAR 3D point clouds. These feature vectors can be completed with local point clouds features re-projected into a Bird’s Eye View (BEV) map which is processed to return axis-aligned regions of interest (ROIs) that encompass the potential obstacles. In fact, it is difficult to estimate parameters such as object orientation if the obstacle is hit by few laser points. These proposals can then be employed for a subsequent system whose role may be to track the potential obstacle in a sequence or estimate finer parameters such as the orientation and the fitted dimensions. This subsequent system will not be covered in this article though.

As another contribution, we also propose a simple augmentation procedure to make networks more robust to point cloud reduction, resulting to a RPN that is able to adapt to different 3D point cloud topologies.

To evaluate the performances of our system, the main tests are performed on KITTI dataset [9]. It is shown that even if the number of 3D points seems to be low to realize some correct predictions, our networks provides accurate regions of interest as shown in Figure 1. Moreover, a more difficult test is realized on the nuScenes dataset [10] to illustrate how our network performs on records with different data from different sensors (LiDAR and camera). Related work on 3D object detection and cross LiDAR methods are reviewed in Section 2. In Section 3, we introduce the different elements that compose our method from the input processing for the training to the used architecture. Experiments and discussions are conducted in Section 4.

## 2 RELATED WORK

In this section, some relevant networks aiming at 3D object detection on point clouds and/or RGB images are firstly introduced. Secondly, methods targeting on the management of point clouds at different resolutions are then presented.

### 2.1 3D Object Detection Methods

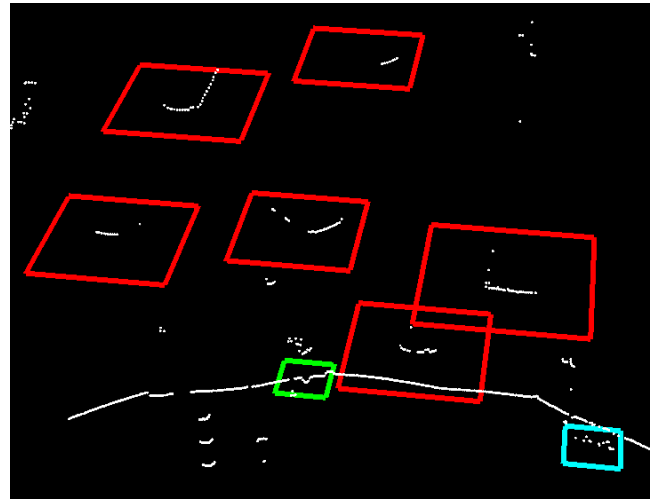
3D object detection methods for autonomous driving can be divided into three main groups depending on which types of data are used: methods that infer 3D properties only from images, methods working exclusively on point clouds and methods using both types of data. Table 1 summarizes these approaches by recalling the raw input data used and the main paradigms existing in the literature. Most of these approaches attempt to identify targets categorized as Car, Pedestrian and Cyclist. In fact, the KITTI dataset, whose benchmarks are centered around those classes, is one of the oldest public dataset allowing easier research on 3D object detection for autonomous driving. In the following paragraphs, those three groups of 3D detection methods are analyzed.

#### 2.1.1 3D Object Detection using 2D Images

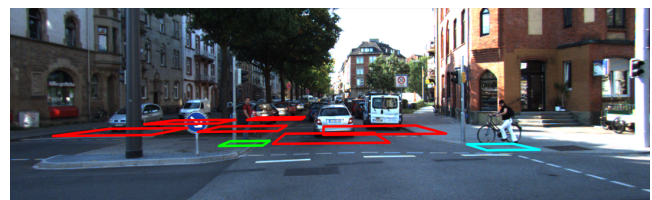
Camera-based 3D object detection methods are generally less precise than LiDAR-based ones due to the loss of depth information in the image creation process. Hence, most of them rely on geometric constraints priors. Here, the focus is given to monocular camera methods.



(a) Input 2D image with projected input point cloud.



(b) Input 3D point cloud and predictions, the boxes are proposals returned by our network, the color of the boxes represents the classes and the score (red: Car, green: Pedestrian, cyan: Cyclist)



(c) Projections of proposals on camera image.

Fig. 1: Example of some results delivered by our network showing that correct proposals can be obtained even with low resolution point clouds.

In [11], a 3D grid is populated with features from the input image by projecting voxels on the image, knowing the camera parameters. To reduce the computational cost, the resulting 3D grid is collapsed on the vertical axis. The authors of [12] train an encoder-decoder architecture for depth estimation. The resulting intermediate features (after the encoder, before the decoder) is then used for 3D object detection. In [13], a two-branch architecture is defined, one using regular convolutions to estimate global features, the other one, called depth aware convolutions, splits the image into row blocks then applies distinct kernels for each bin. The main assumption is that each row block can be associated to a discretized depth due to perspective effects (for example, lower rows often represent road and close objects) and then a different operation for each depth bin is applied. In [14], a 2D object detection method is followed by a 3D object detection one. However, their loss function splits the box parameters into groups to simplify the optimization process.

TABLE 1: Summary of published networks aiming at 3D object detection from point clouds and/or RGB images. An overview of the state of experimental evaluation of methods useful for autonomous driving.

Reference	Raw Input Data	Raw Data Processing	Overview	Object Types	Dataset(s) used
OFT [11]	RGB Image	-	Resnet Backbone, projection of 3D voxels on image feature maps, each 3D assigned with features inside the projection, then Voxelnet-like processing	Cars	KITTI
M3D-RPN [13]	RGB Image	-	DenseNet Backbone then 2 branches: (1) global feature extraction on whole image, (2) local "Depth-Aware" feature extractions. Horizontally sliced image. Each slice is fed to its own convolution	Car, Pedestrian, Cyclist	KITTI
MonoDIS [14]	RGB Image	-	ResNet Backbone, 2D and 3D heads, box parameters divided into groups for a better convergence	Car, Pedestrian, Cyclist	KITTI
CubifAE-3D [12]	RGB Image	-	Multiple trainings: (1) depth estimation through encoder-decoder, (2) depth latent space for 3D detection	Car, Pedestrian, Cyclist and others	KITTI, nuScenes, KITTI Virtual 2
BirdNet [15]	Point Cloud	Discretization into BEV 3-channel image (height, density, reflectance)	Faster RCNN-like network	Car, Pedestrian, Cyclist	KITTI
Complex-YOLO [16]	Point Cloud	Discretization into BEV 3-channel image (height, density, reflectance)	YOLO-like network, complex angles for regression	Car, Pedestrian, Cyclist	KITTI
VoxelNet [17]	Point Cloud	3D voxelization	Learned voxel encoding for each voxel, 3D convolutions to flatten on the vertical axis then RPN	Car, Pedestrian, Cyclist	KITTI
SECOND [1]	Point Cloud	3D voxelization	Learned voxel Encoding, sparse 3D convolution to reduce the computational burden, RPN	Car, Pedestrian, Cyclist	KITTI (nuScenes thereafter)
PointPillars [18]	Point Cloud	Column voxelization (no slices on vertical axis)	Learned voxel encoding, 2D convolutions, RPN	Car, Pedestrian, Cyclist	KITTI, nuScenes
OHS [19]	Point Cloud	3D voxelization, voxels represented by the mean content	Objects as sets of hotspots (non empty voxels belonging to an object), architecture inspired by SECOND or PointPillars according to the dataset	Car, Pedestrian, Cyclist and others	KITTI, nuScenes
PointRCNN [4]	Point Cloud	-	Two-stage method: (1) 3D proposal generation through point cloud segmentation, each foreground point generating its own 3D proposal, (2) 3D box refinement	Car, Pedestrian, Cyclist	KITTI
Fast Point RCNN [5]	Point Cloud	3D voxelization	Two-stage method: (1) 3D region proposal through VoxelNet architecture, (2) pooling on VoxelNet's feature maps, fusion with the corresponding section of point cloud, refinement network on pooled and augmented point cloud	Car, Pedestrian, Cyclist	KITTI
CenterPoint [20]	Point Cloud	3D or column voxelization	Objects represented by their center on the classification map, architecture inspired by VoxelNet & PointPillars	nuScenes classes	nuScenes
PV-RCNN [21]	Point Cloud	3D Voxelization + furthest point sampling to extract keypoints	Two-stage detection: (1) architecture inspired by SECOND for the region proposal, the 3D feature maps sampled at multi-scales using the computed keypoints, (2) RoI-Grid Pooling on the keypoints then Refinement Network	Car, Cyclist	KITTI
Part-A <sup>2</sup> Net [22]	Point Cloud	-	Two-stage detection: (1) point cloud semantic segmentation, part estimation for positive 3D points then 3D proposals, (2) point cloud pooling then refinement network to aggregate the estimated parts	Car, Pedestrian, Cyclist	KITTI
MV3D [23]	Point Cloud, RGB image	Discretization into BEV 3-channel image (height, density, reflectance) and Cylindrical projection	Two-stage detector: (1) BEV generates 3D proposals, (2) 3D proposals are projected on the BEV, the RGB image and on the cylindrical view, features from the 3 feature maps (each view) are pooled then merged to refine the boxes	Car	KITTI
Frustum PointNet [7]	Point Cloud, RGB image	-	2D detector on the image to create their 3D frustum, for each result, the 3D points inside the frustum used to estimate the corresponding 3D box with an architecture similar to PointNet++	Car, Pedestrian, Cyclist	KITTI
AVOD [24]	Point Cloud, RGB	Discretization into BEV 3-channel image (height, density, reflectance)	Two-stage detector: (1) BEV and RGB images merged to generate 3D proposals (2) 3D proposals are projected on the BEV and the RGB image feature maps, the corresponding features are pooled then merged to refine the 3D boxes	Car, Pedestrian, Cyclist	KITTI
PointFusion [25]	Point Cloud, RGB image	-	2D detector to extract 2D crop and 3D frustum, 2D crop and corresponding point cloud processed by a ResNet and a PointNet, respectively. Features merged to estimate a refined 3D box	Car, Pedestrian, Cyclist	KITTI, SUN-RGBD
ContFusion [26]	Point Cloud, RGB image	-	2D feature extraction, feature sampling through continuous convolution with the point cloud, reprojection of the sampled features on a BEV then 3D box prediction	Car	KITTI, TOR4D (private)
IPOD [27]	Point Cloud, RGB image	2D Semantic Segmentation	3 parts: (1) using the 2D segmentation, all the 3D background points are discarded and proposals are generated from the remaining points, (2) a backbone network extracts local and global features from the whole point cloud, (3) the features are extracted from the proposals and used in a refinement network	Car, Pedestrian, Cyclist	KITTI
Frustum ConvNet [28]	Point Cloud, RGB image	-	2D detector on the image to create their 3D frustum, for each result, the part of the point cloud inside the frustum is kept and voxelized along the frustum axis, convolutions are used along this axis to estimate the 3D box	Car, Pedestrian, Cyclist	KITTI
PointPainting [6]	Point Cloud, RGB image	2D Semantic Segmentation	Point features (3D coordinates, reflectance) concatenated with the score given by 2D segmentation. Experiments on multiple detectors (PointRCNN, PointPillars, etc.)	Car, Pedestrian, Cyclist	KITTI, nuScenes
MVX-Net [29]	Point Cloud, RGB image	3D Voxelization	VoxelNet used for the 3D detection and Backbone Faster RCNN for the 2D feature maps, 2 fusion methods tested: (1) 2D features sampled on point level and merged before voxel encoder, (2) 2D features sampled on voxel level and merged after voxel encoder	Car	KITTI
MMF [30]	Point Cloud, RGB image	3D Voxelization	Two-stage detector: (1) RGB image processed to generate intermediate feature maps and a depth map. These maps are merged with LiDAR features to generate 3D proposals. (2) LiDAR and RGB feature maps are pooled and merged to refine the estimated boxes	Car (main)	KITTI, TOR4D (private)

### 2.1.2 Point Cloud-based Methods

These methods only use 3D point clouds provided by 3D LiDAR sensors. This category can be divided into two subgroups: grid-based and point-based methods.

#### Grid-based Methods

The main achievements obtained in object detection occurred on structured data, mainly RGB images. Hence, the main idea of grid-based methods consists in turning the 3D point cloud into structured data to allow the use of concepts and operators which were successfully applied in 2D image processing such as convolutions. The main drawback is that the precision depends on the discretization of the grid. Some methods are based on existing 2D architectures to extract detections from Bird Eye’s View pseudo images. BirdNet [15] and Complex YOLO [16] are based on Faster-RCNN [31] and YOLO [32], [33], respectively. Their corresponding networks are applied on 3-channels pseudo-image made by the concatenation of a height map, a reflectance map and a density map. VoxelNet [17] was a major milestone. In their paper, the authors describe an architecture including encoding voxels features through PointNet-like methods. The encoded grid is given to 3D dense convolutions and afterwards to 2D convolutions in order to return the selected prior boxes and their correction. However, the use of 3D dense convolutions on a large 3D grid is slow and expensive. SECOND [1] rectifies this by applying sparse convolutions [34] on the grid. PointPillars [18] extends the concept by using directly columns in a 2.5D pseudo image instead of voxels in a 3D grid in order to speed up the computation. Voxel-FPN [35], inspired by the Feature Pyramid Networks [36], uses voxel grids with different resolutions to encode voxels at different scales. Anchor-free methods, assimilating object detection to keypoint detection [37], [38] have also been transposed to 3D object detection [19], [20]. The main goal is not to change the input data representation but the output format, as detections are no more related to prior boxes.

#### Point-based Methods

Contrary to grid-based methods, point-based methods aim to deal at some stage with raw point clouds, directly. This paradigm can be applied for the whole method or jointly with grid representations. Moreover, most of these methods are two-stage detectors. PointRCNN [4] adopts a two-stage approach: a first stage generates proposals from foreground point segmentation, a second phase refines the proposals to estimate targeted boxes. Fast PointRCNN [5] and PV-RCNN [21] employ a VoxelNet-like to generate proposals that are processed by PointNet-like networks. Part-A<sup>2</sup> [22] directly estimates object parts (top left, bottom right, etc.) from point cloud in the first stage to improve the 3D box refinement stage.

### 2.1.3 3D Object Detection using Multi-Sensor Fusion

Contrary to the aforementioned methods that exploit only one sensor, the ones presented in the following section focus on camera-LiDAR data fusion to localize the surrounding objects. These methods can be divided into two sub-groups. The first group makes use of both sensor data within the same system. The second group rather employs outputs from existing and pre-trained 2D methods as priors or inputs for methods that focus on point clouds. Both groups are introduced in the following paragraphs.

#### Parallel Flows

These methods generally use images as a second input to exploit complementary nature of data. MV3D [23] and AVOD [24] belong to methods that simultaneously process images and point

clouds to extract intermediate proposal. MV3D [23] generates 3D proposals from a LiDAR Bird Eye’s View image and then, projects them onto the LiDAR BEV, a LiDAR front view and an RGB image. Features inside the projection of each modality are extracted through ROI pooling and merged to estimate final boxes. AVOD [24] extends the idea by projecting all pre-built prior boxes on high-resolution feature maps from LiDAR BEV and RGB images. MVX-Net [29] add pooled features from RGB feature maps into voxels that are used on a VoxelNet. The method described in [26] takes advantage of leveraging continuous convolutions to merge feature maps from each sensor. The authors of [30] improve this architecture by adding related tasks such as ground estimation and depth completion to boost the 3D refinement sub-network.

#### Sequential Streams

2D processing systems have become more mature. Contrary to above-mentioned, the methods introduced in this paragraph operate sequentially and are 2D driven since they exploit results from RGB processing as filters on point cloud. Frustum PointNet [7], Frustum Convnets [28] and PointFusion [25] exploit results from a 2D detector to extract points that fall inside each detection and then reduce the search space for each object detected by the image detector. The frustums are then processed to precisely localize objects. IPOD [27] removes the background 3D points by exploiting a segmentation map from RGB camera images. Each foreground point is used as a location for prior boxes and then processed afterwards. In [6], the authors show the performances improvement on several LiDAR detectors only by integrating the semantic information from a segmentation map on the input.

## 2.2 Point Cloud-based Resolution-Agnostic Deep Learning

To the best of our knowledge, even if domain adaptation has become an active research field on images, few works on domain adaptation or portability have been done on 3D point clouds, especially on outdoor sensor data. As illustrated in [39], each 3D LiDAR has its own features about range, point distribution, data coherency on disturbed conditions. The authors of [40] perform a deep analysis of the performance of their architecture for semantic segmentation of point clouds from a 32-layer and a 128-layer LiDAR. 3D Domain Adaptation is especially studied and analyzed on 3D CAD (Computer-Aided Design) objects datasets such as ModelNet [41] and dense indoor point clouds. Studies on open scenes are less usual and most of them targets the semantic segmentation of point clouds. In [42], a shared representation is learned in a self-supervised fashion through the reconstruction of deformed 3D point clouds. PointDAN [43] designed an architecture to learn cross domain local and global features to align objects from two distinct distributions. Some methods such as [44] employ Generative Adversarial Networks (GAN) to close the gap between synthetic data and real-world data. In [45], the authors propose a point cloud completion method by assimilating the task as the reconstruction of the underlying surface. A semantic segmentation network is then trained from the reconstructed surface that serves as the new canonical domain.

Our method does not directly aim at LiDAR domain adaptation. Instead, the use of RGB data and our augmentation procedure enforce some aspects of the network that makes it more resilient to point cloud resolution variations.

### 3 LIDAR-CAMERA DATA FUSION REGION PROPOSAL NETWORK REGARDLESS OF POINT CLOUD RESOLUTION

In this paper, we propose an end-to-end trainable method for a region proposal network detection. The Region Proposal Network (RPN) takes RGB images and point cloud as inputs. The objective is to deliver a Bird’s Eye View (BEV) Axis-Aligned Bounding Boxes (AABB) for the objects inside the search space that can be used in a subsequent refinement network in order to accurately regress the Oriented Bounding Boxes (OBB). As raw images are also available, and contrary to many two-stage methods, a semantic classification is performed on proposals. In this section, the chosen inputs jointly with the architecture of the network and the output generation procedure are described.

#### 3.1 LiDAR Data Preprocessing

This section presents the set of operations applied on the 3D LiDAR point cloud to produce a voxel-based representation. The voxelization paradigm introduced in [18] is used. The point cloud is turned into columns voxels with no vertical discretization compared to a 3D voxel grid. This way, a BEV grid/map whose each non-zero pixel is assigned to a non-empty voxel is generated. The terms “pixel” and “voxel” are used interchangeably when referred to the BEV image.

The  $x$ -axis is oriented forwards, the  $y$ -axis is oriented to the left and the  $z$ -axis is oriented upwards. A 3D point cloud is defined as a set  $\mathbf{P} = \{[x_i, y_i, z_i]^T \in \mathbb{R}^3\}_{i \in 1 \dots N}$  with  $(x_i, y_i, z_i)$  the location of the  $i$ -th point in the 3D space. The search space is restricted to the interval  $[x_{min}, x_{max}]$  on the  $x$  axis and  $[y_{min}, y_{max}]$  on the  $y$  axis. This point cloud is discretized and grouped into column voxels of size  $(s_x^{in}, s_y^{in})$ . The resulting BEV grid contains  $n_x^{in} \times n_y^{in}$  voxels where

$$n_x^{in} = \left\lfloor \frac{x_{max} - x_{min}}{s_x^{in}} \right\rfloor, n_y^{in} = \left\lfloor \frac{y_{max} - y_{min}}{s_y^{in}} \right\rfloor.$$

The LiDAR points are grouped according to the voxel they belong to. The number of points in a voxel is variable and depends on many parameters such as the topology of the scene, the distance of the voxel from the sensor, the used sensor, and the pose of the LiDAR towards the scene. For each non-empty voxel, a Normal Distribution Transform (NDT) [46] is operated on the points inside the voxel. The Normal Distribution Transform is a simple method that turns a set of points into a multivariate Gaussian function. For 3D points, a voxel is then represented by a feature voxel which is at least a vector of size 9 composed by:

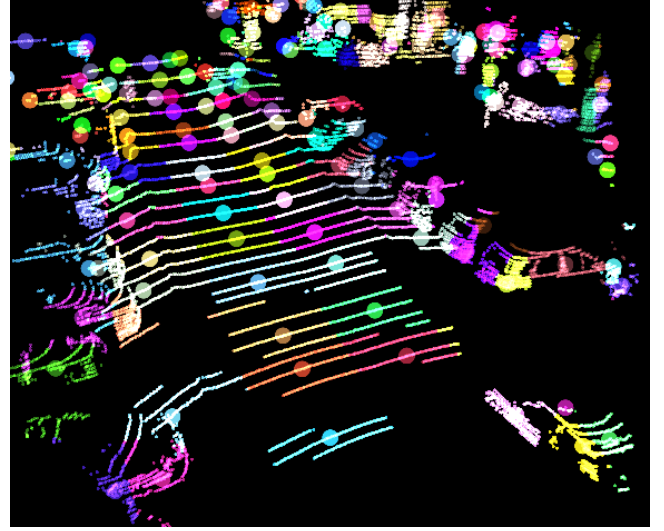
- the mean  $\boldsymbol{\mu} = (\mu_x, \mu_y, \mu_z)^T \in \mathbb{R}^3$ ;
- the symmetric covariance matrix  $\boldsymbol{\Sigma} \in \mathbb{R}^{3 \times 3}$ .

The six extreme coordinates of the 3D points inside the voxel are also included in the feature voxel. Therefore, the 3D information representing the voxel is encoded as a vector of  $3 + 6 + 6 = 15$  dimensions.

Aside from the feature vector, a “Main Point” is defined for each voxel. For  $\chi = \{\mathbf{x}_1, \dots, \mathbf{x}_n\}$  the 3D points inside the voxel,  $\bar{\mathbf{x}}$  the mean point,  $d$  the Euclidean distance, the “3D Main Point”  $\mathbf{x}_M$  is defined as

$$\mathbf{x}_M = \arg \min_{y \in \chi} d(y - \bar{\mathbf{x}}). \quad (1)$$

This point is representative of the content of the voxel while belonging to the original set of points. The projections of the estimated main points are computed so each voxel is represented by one point on the image frame as illustrated in Figure 2.



(a) Outputs of voxelization, each large point is a main point.



(b) Projection of the main points on the RGB image.

Fig. 2: Relationships between voxels on image frame and BEV frame. One voxel is represented with the same color on each figure. The BEV map is low resolution for better readability.

#### 3.2 Proposed Network Architecture

The architecture of the RPN can be broken down into two sub-parts: an image feature extractor operating on the image frame and a BEV estimator running on the BEV frame. Each block is described in the following paragraphs. The global structure of the RPN is described in Figure 3.

##### 3.2.1 Image Feature Extractor

This network produces a feature map from the input RGB image. A Feature Pyramid Network (FPN) architecture has been adopted to extract information from feature maps at multiple scales. First, the image is processed by a core network which returns three feature maps at different scales. These maps are given to a head network (named “RGB feature head” in Figure 3) whose task is to merge these feature maps into one. The resulting map is up-sampled by a factor 4 (the block “Up4”). Using the projection of each voxel’s main point, the feature map is sampled and each voxel is assigned with the extracted feature vector.

##### 3.2.2 BEV Estimator

Each voxel has now a feature vector from the image feature encoder and a feature vector from the 3D point cloud. Both are concatenated and transformed by linear layers. Knowing their location on the BEV grid, it can be filled with the resulting feature vectors. A second FPN core network is applied on the BEV feature grid. The resulting feature maps are then given to two different head networks, one for the classification, the other for the regression. The use of FPN is motivated by the fact that

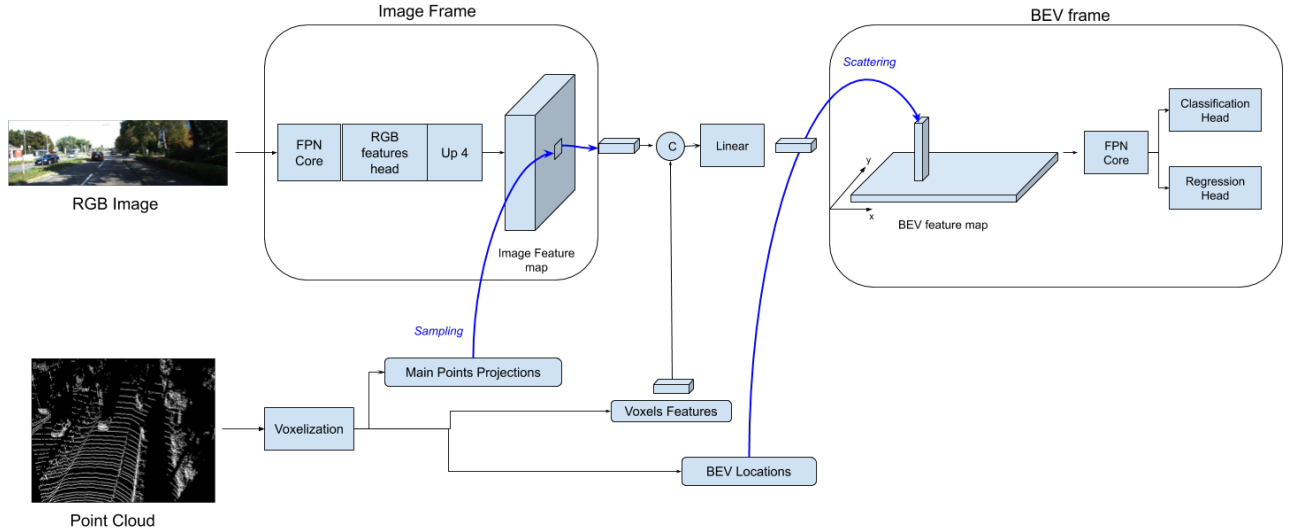


Fig. 3: Overview of the proposed network architecture.

objects from different categories may not be represented with the same scale on both frames (close/far objects in the image frame, small/large objects in the BEV frame). Feature Pyramid Networks manage well objects with various apparent sizes as multi-scale features maps are generated.

### 3.3 Network Output

Contrary to many methods defining prior boxes with various sizes and orientation located in fixed positions, an anchor-free approach inspired by [37] is employed here to represent the objects where each predicted one is only described by its center. In fact, anchors-based methods require a set of hyper-parameters specifically tuned to work correctly (size of anchors, IoU threshold to define a positive anchor, etc.). Anchor-free method removes this constraint, allowing to reduce the number of critical parameters that may greatly affect the training process.

In common datasets, 3D obstacles are represented by a position  $(x, y, z)$ , dimensions  $(h, w, l)$  and an orientation  $\theta$ . The orientation is restrained to the vertical axis for urban and peri-urban scenes. However, our goal here is to extract regions with defined limits and location but not the oriented boxes. At this stage, estimating refined boxes is not suitable for two main reasons:

- RGB images provide mainly appearance features but estimating 3D spatial features from a projection is a difficult task. Advances in 3D related tasks with monocular setups are still less precise than their counterparts using range sensors;
- even if the pixels of an image are tightly packed, the sampling from the voxelization may not follow the resolution of the image. Some pixels are skipped and then the complete information is not obtainable.

In that sense, the regions of interest are defined as cuboids with a specified side  $s$  and the position of their center. The cuboid must be large enough to encompass an important part of an object of interest, but must not include other interfering objects.

The RPN returns two maps: A classification one and a regression one, both having the same size. Each pixel of both map represents a cuboid similar to a prior/anchor box, the first

map gives its confidence score, its category and an approximate location while the second map gives the correction on the position and the predicted side. The extraction of top proposals is summed up to the identification of local maxima in the classification map and the gathering of the estimated corrections on the regression map at the same locations.

### 3.4 Training

#### 3.4.1 Ground Truth Formatting

Each ground truth object  $i$  is defined by a semantic category and its box parameters  $(x_i, y_i, z_i, h_i, w_i, l_i, \theta_i)$  with  $(x_i, y_i, z_i)$  its position,  $(h_i, w_i, l_i)$  its dimensions and  $\theta_i$  its orientation. Our RPN has to estimate coarse AABB proposals that surround these ground truth objects.

Ground truth maps are formatted using a process inspired by [37]. Each label is represented by a Gaussian function whose mean is the center of the object. A voxel is called positive if its ground truth value is 1 (the center of the object belongs to this voxel). One label is then assigned to one voxel in the classification map.

Concerning the regression map, let us denote  $\Delta x$  the first channel,  $\Delta y$  the second one and  $\Delta s$  the third one representing the sides of proposals. Voxels are defined according to a static grid with fixed position and each voxel on the classification map represents a portion on the metric space. For the ground truth object  $i$ , its associated voxel, whose center is located at  $(\tilde{x}_i, \tilde{y}_i)$  in the metric space and at  $(u, v)$  on the regression map, the corresponding target for the regression is defined as:

$$\begin{aligned} \Delta x(u, v) &= \tilde{x}_i - x_i, \\ \Delta y(u, v) &= \tilde{y}_i - y_i, \\ \Delta s(u, v) &= \sqrt{(w_i)^2 + (l_i)^2}. \end{aligned} \quad (2)$$

#### 3.4.2 Loss Functions

The RPN loss is a sum of two losses:

$$L = \gamma_{cls} L^{cls} + \gamma_{reg} L^{reg} \quad (3)$$

with  $L^{cls}$ ,  $L^{reg}$  the losses related to classification and parameter regression,  $\gamma_{cls}$ ,  $\gamma_{reg}$  their respective weights.

$L^{cls}$  being a pixel oriented focal loss on all elements (voxels) for the scene level:

$$L^{cls} = -\frac{1}{N} \sum_{uvc} \begin{cases} (1 - \hat{p}_{uvc})^\alpha \log(\hat{p}_{uvc}) & \text{if } p_{uvc} = 1 \\ (1 - p_{uvc})^\beta (\hat{p}_{uvc})^\alpha \log(1 - \hat{p}_{uvc}) & \text{else} \end{cases} \quad (4)$$

with  $\alpha, \beta$  being the hyper parameters that control the influence of positive and negative voxels on the loss.  $p_{uvc}, \hat{p}_{uvc}$  are respectively the ground truth and the prediction of the voxel located in  $(u, v)$  in the classification map for the class  $c$ .  $N$  is the number of positive voxels in the ground truth map ( $p_{uvc} = 1$ ).

$L^{reg}$  is defined as follows:

$$L^{reg} = -\frac{1}{N} \sum_{u_{pos} v_{pos}} \begin{aligned} & SL1(\Delta x_{u_{pos} v_{pos}}, \hat{\Delta x}_{u_{pos} v_{pos}}) \\ & + SL1(\Delta y_{u_{pos} v_{pos}}, \hat{\Delta y}_{u_{pos} v_{pos}}) \\ & + SL1(\Delta s_{u_{pos} v_{pos}}, \hat{\Delta s}_{u_{pos} v_{pos}}) \end{aligned} \quad (5)$$

with  $SL1(.,.)$  denoting the Smooth  $L1$  loss,  $(u_{pos}, v_{pos})$  the locations of the positive voxels in the regression maps,  $(\Delta x, \Delta y, \Delta s)$  the target maps defined earlier,  $(\hat{\Delta x}, \hat{\Delta y}, \hat{\Delta s})$  the predicted maps.

### 3.5 Data Augmentation

This section describes the data augmentation strategies proposed for the training. In autonomous driving field, the most common LiDAR sensors used are rotating mechanical sensors, delivering 3D points from one emission location in a layered manner. Points from the same layer share the same latitude in a spherical frame centered on the sensor. The different layers of the point cloud are supposed to be registered. Then for each sample, some layers are randomly discarded until a specific percentage of the point cloud layers remains.

Generally, images of open scenes are acquired with a large field of view and high resolution as well. However, training with such resolutions is cumbersome due to memory consumption aspects. Indeed, during the training stage, gradients have to be computed on each pixel at each layer of the neural network. GPUs have to store images and all tensors computed by the network from them. In order to reduce these phenomena, a random cropping strategy which is mostly used for segmentation methods is adopted. Here, we set  $(W_{patch}, H_{patch})$  for the width and the height of the cropped region, respectively. The RGB encoder being fully convolutional, feeding it on test time with an input with larger resolution is possible as long as the image stays in the same domain (lighting conditions, camera noise, etc.).

Some categories of labels belong to the minority of labels or are missing in most of the training samples. Purely random cropping may lead to a majority of background or will mainly include the most common category. Thus, the cropped region is chosen according to the content of the scene:

- if the scene contains at least one label, one of them can be randomly selected (Figure 4a). A cropping region is then defined around the selected label (Figure 4b) and a random shift is applied so the selected label is not centered on the crop (Figure 4c);
- if the sample does not contain labels, crops are selected randomly.

Even if the label is selected randomly, the probabilities between each label are not uniform and depend on one or multiple criteria. Random horizontal flips and color jittering are applied on the cropped patch.

To keep data consistency, every point whose projection is outside the cropping region is discarded leading, for the point cloud and for the BEV image, to a much smaller field of view. Examples of the resulting RGB and 3D input data are shown in Figure 4e and Figure 4f, respectively.



(a) Selected label.



(b) Crop region centered.



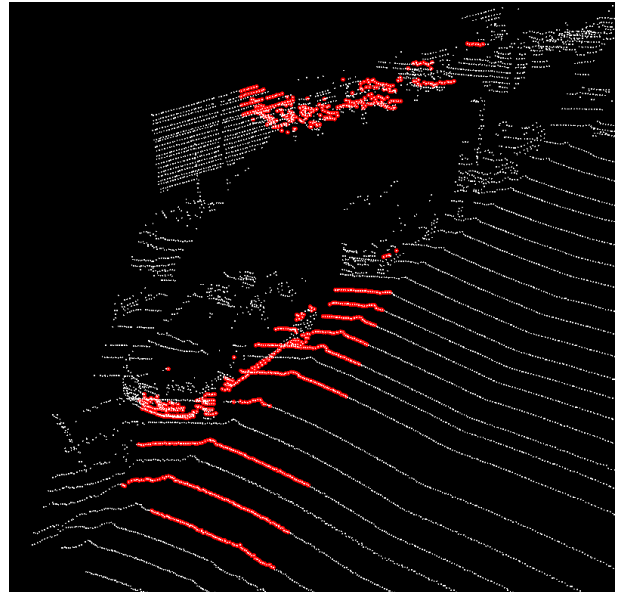
(c) Crop region shifted.



(d) Original RGB Image



(e) Input RGB Image



(f) Original point cloud (white) and Input point cloud (red)

Fig. 4: Example of KITTI inputs for the training.

## 4 EXPERIMENTS AND RESULTS

In this section, we first introduce the two datasets used in this study, KITTI and nuScenes. The next section details the chosen parameters for the proposed network and the training stage. Thereafter, the conducted experiments and their results are described. Finally, some ablation studies are presented to justify the choices unrelated to the considered datasets.

### 4.1 Datasets

#### 4.1.1 KITTI

KITTI [9] is a public dataset for autonomous driving tasks available since 2012 that contains data recorded by an equipped vehicle around Karlsruhe, in Germany. The embedded sensors include a 64-layer LiDAR on the top of the vehicle and two front color cameras. In this study, only the subset dedicated to 3D object detection is used. This dataset contains 7481 annotated training samples and 7518 testing samples, each sample consists of a panoramic 3D point cloud, the RGB images from each camera, the calibration parameters, all being synchronized. The annotations are only defined in the camera’s field. As labels in the testing samples are not publicly available, the original samples are split into 3741 training samples and 3740 validation samples.

#### 4.1.2 nuScenes

nuScenes [10] is another public dataset first released in 2019, mainly for object detection. Samples were collected in Boston and Singapore. The acquisition vehicle boards 32-layer LiDAR sensor, 6 color cameras, each one facing a different direction, 5 radars, a GPS and an IMU. The dataset exists in two versions:

- a complete version: it contains 1000 scenes split into 850 training scenes and 150 testing scenes;
- a mini version: it contains 10 scenes.

Each scene is 20 s long. Samples are annotated at 2 Hz. Intermediate point clouds called “Sweeps” are defined between annotated samples. The dataset defines 23 different categories of objects.

#### 4.1.3 Experimental Setup

All the presented networks are trained on the KITTI train set. The following results are computed either on the validation set or on the scenes of nuScenes Mini to keep the same order of magnitude on the number of samples. A common technique used for nuScenes dataset is, for one sample, to accumulate some previous sweeps, not labeled, and augment each point of the accumulated cloud with its original timestamp, in order to get a denser point cloud. No sweeps are available in the KITTI dataset, thus only the nuScenes annotated point clouds are used. Moreover, all the KITTI scenes were captured on daylight. Hence, we focus on the nuScenes sequences that were recorded on similar conditions and skip night sequences as numerous new disturbances occur on the image (lens flares due to streetlights and car lamps, higher noise, etc.). Finally, if KITTI object detection benchmarks focus on three main classes, nuScenes meanwhile defines more categories. Hence, in order to allow the comparison between results on both datasets, we selected the nuScenes categories that are the closest to the KITTI classes. Table 2 illustrates the established correspondences between classes from both datasets.

TABLE 2: Established correspondences between KITTI classes and nuScenes categories.

KITTI	nuScenes
Car (and Van)	Car
Pedestrian	Pedestrian
Cyclist	Bicycle attribute “with rider”

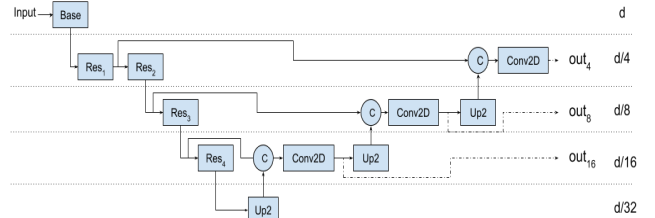
Concerning the nuScenes dataset, we focus the daylight scenes from the version “Mini”. This subset counted 4539 Car labels, 2826 Pedestrian labels and 75 Cyclist labels.

### 4.2 Implementation Details

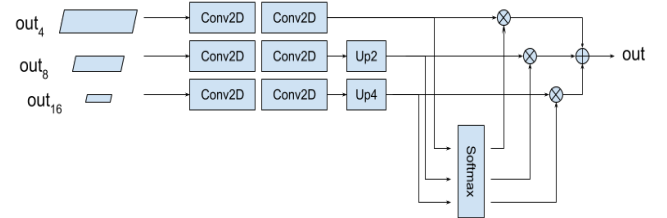
In this section, details on the network parameters and on the training procedure are provided.

#### 4.2.1 Details on the Network Architecture

As illustrated in Figure 3, the proposed network is composed of two main blocks, an image feature extractor and a BEV estimator. Each of them is composed of instances of the two sub-networks, a FPN core (Figure 5a) whose role is to extract three feature maps at different scales and a FPN head (Figure 5b), in charge of merging those features maps into one output. Blocks labeled as “RGB feature head”, “Classification head” and “Regression head” are all instances of a FPN head. Their structures are detailed in Figure 5.



(a) FPN Core. Blocks named  $Res_i$  are Resnet Blocks. Ratios on the right indicate the size of the feature map at each stage.



(b) FPN Head.

Fig. 5: Details of RPN sub-networks.

$\text{Conv2D}(c_{in}, c_{out}, k, s, p)$  refers to a 2D convolution operator with  $c_{in}$ ,  $c_{out}$  the number of input and output channels,  $k$  the kernel size,  $s$  the stride,  $p$  the padding. Likewise,  $\text{MaxPool}(k, s, p)$  denotes a Max Pooling operator,  $k$  the kernel size,  $s$  the stride,  $p$  the padding. Blocks named “Up2” and “Up4” represent an up-sampling with a factor 2 and 4, respectively.

#### Image Feature Extractor

The block named “Base” used in the Image Feature Extractor’s Core is composed of a  $\text{Conv2D}(3, 64, 7, 2, 3)$ , a batch normalization, a ReLU activation and a  $\text{MaxPooling}(3, 2, 1)$ . Block labels  $Res_i$  comes from a ResNet18 architecture. On

the FPN core (Figure 5a),  $out_{16}$ ,  $out_8$ ,  $out_4$  are produced by Conv2D(768, 256, 1, 1, 0), Conv2D(384, 128, 1, 1, 0) and Conv2D(192, 64, 1, 1, 0), respectively. Concerning the RGB feature head as illustrated in Figure 5b, each feature map are given to their own Conv2D( $c_{dim}$ , 64, 3, 1, 1) followed by a Conv2D(64,  $c_{task}$ , 1, 1, 0), where  $c_{dim}$  depends on the numbers of channels of the feature map and  $c_{task}$ . For  $out_{16}$ ,  $out_8$ ,  $out_4$ ,  $c_{dim}$  is set to 256, 128 and 64, respectively.  $c_{task}$  is set to 64.

### BEV Estimator

The proposed architecture is close to the one described in the previous paragraph entitled ‘‘Image Feature Extractor’’. As a result, only the differences between Image Features Extractor architecture and the BEV Estimator structure are described. The first convolution in the ‘‘Base’’ block is replaced by a Conv2D(64, 64, 7, 2, 3). Classification and Regression heads have the same structure as the RGB feature head, only  $c_{task}$  varies. For the classification,  $c_{task} = 3$  is selected for the studied classes: Car, Pedestrian and Cyclist. For the regression,  $c_{task}$  is assigned to 3 for estimating  $(x, y, s)$ .

Table 3 defines the borders of the search space and the dimensions of the input maps (from the voxelization) and output maps (the different head sub-networks).

TABLE 3: Global parameters (train and test).

Parameters	Values
$(x_{min}, x_{max})$	(0 m, 50 m)
$(y_{min}, y_{max})$	(−25 m, 25 m)
$(s_x^{in}, s_y^{in})$	(0.0625 m, 0.0625 m)
$(n_x^{in}, n_y^{in})$	(800, 800)
$(s_x^{out}, s_y^{out})$	(0.25 m, 0.25 m)
$(n_x^{out}, n_y^{out})$	(200, 200)

The values displayed in Table 3, are selected according to the labels existing on the KITTI and the nuScenes datasets. All data are annotated between 0 and 50 m around the sensor, except for cars in KITTI which are annotated until 80 m. Pedestrians are the smallest targets studied in this work, the output voxel size is selected, so they can cover at least one voxel on the output maps.

#### 4.2.2 Training Stage Parameters

The focus criteria for the patch extraction in the data augmentation is the 3D volume: The smaller the target is, the greater the probabilities to be selected are. As small objects are harder to detect, a special focus allows to improve the attention of the network to details. Dimensions of the RGB patches ( $W_{patch}, H_{patch}$ ) are (256, 256). Between 20% and 40% of the layers from point clouds are kept.  $(\gamma_{cls}, \gamma_{reg})$  are defined as (1, 1). For the focal loss,  $(\alpha, \beta)$  are defined as (2, 4). These values come from an improved implementation of [1]. All models are trained for 100 epochs using an Adam optimizer and a one-cycle learning rate scheduler with a maximum learning rate set to 0.001.

## 4.3 Experiments Conditions Description

### 4.3.1 Three Configurations of the Proposed Network

In order to highlight the relevance of the proposed network, its performances are presented and discussed under multiple configurations and training setups. For that purpose, three configurations of R-AGNO-RPN are trained and studied according to the considered sensors:

- an image with 3D Point cloud RPN, its architecture is detailed in Figure 3, the prefix *Cam3D\_* is employed to identify it;
- an image RPN, which has the same architecture as the previous one but the voxel features are not retained. However, the point cloud information required for the sampling and the scattering operations are still used. This experiment is named with the prefix *Cam\_* in the following sections;
- a LiDAR-based RPN, the image frame part is removed, only the point cloud features and the voxels locations are used, named with the prefix *3D\_* in the following sections.

These three configurations are trained according to two following procedures:

- the network is trained from all the point cloud layers, identified with the suffix *\_all*;
- the network is trained from randomly selected point cloud layers, between 20% and 40% of the layers are kept, identified with the suffix *\_few*.

For the inference, only the 20 top proposals are selected as the greatest part of scenes contain at most 15 labels.

### 4.3.2 Comparison with a State-of-the-Art Network

Still with the aim of highlighting the strength of the proposed algorithm, we also propose to carry out a comparative study with a well-known reference state-of-the-art method, the PointPillars network [18] which has popularized the use of column voxels. However, in order to conduct the study under comparable conditions, some modifications were implemented:

- the three classes are simultaneously managed. In the original paper [18], a set of weights was especially trained for Cars and another one was optimized to manage Pedestrians and Cyclists;
- to match with our outputs, only axis-aligned boxes are returned. By removing the estimation of some parameters such as the orientation during the training, the loss and the network focus mainly on the localization;
- the anchors are modified to become cuboids whose side is the diagonal of the original prior boxes.

The PointPillars network is also trained with original data and altered data. These two experiments are labeled *PP\_all* and *PP\_few*, respectively. Everything else stayed the same as in the original paper (network architecture, training process, etc.). The term ‘‘Number Layers’’ refers to the number of layers in the point cloud used at test time.

## 4.4 Experimental Results Analysis

We evaluate in this section our proposed networks through Average Precision (AP) on the validation set. AP takes into account the false positives and prediction scores to reflect how close the results are from the labels. Even if the developed network aims to be the first stage of a two-stage detector, AP gives an indication on how confident the network is.

AP is computed on AABB (axis-aligned bounding boxes). AP is computed for all classes with an IoU threshold of 0.5.

The results on average precision are illustrated in Table 4 and Figure 6 represents the evolution of AP for different trainings with the number of layers of input point clouds on testing phase. The layers are selected in a deterministic way so all the experiments can be realized under the same conditions.

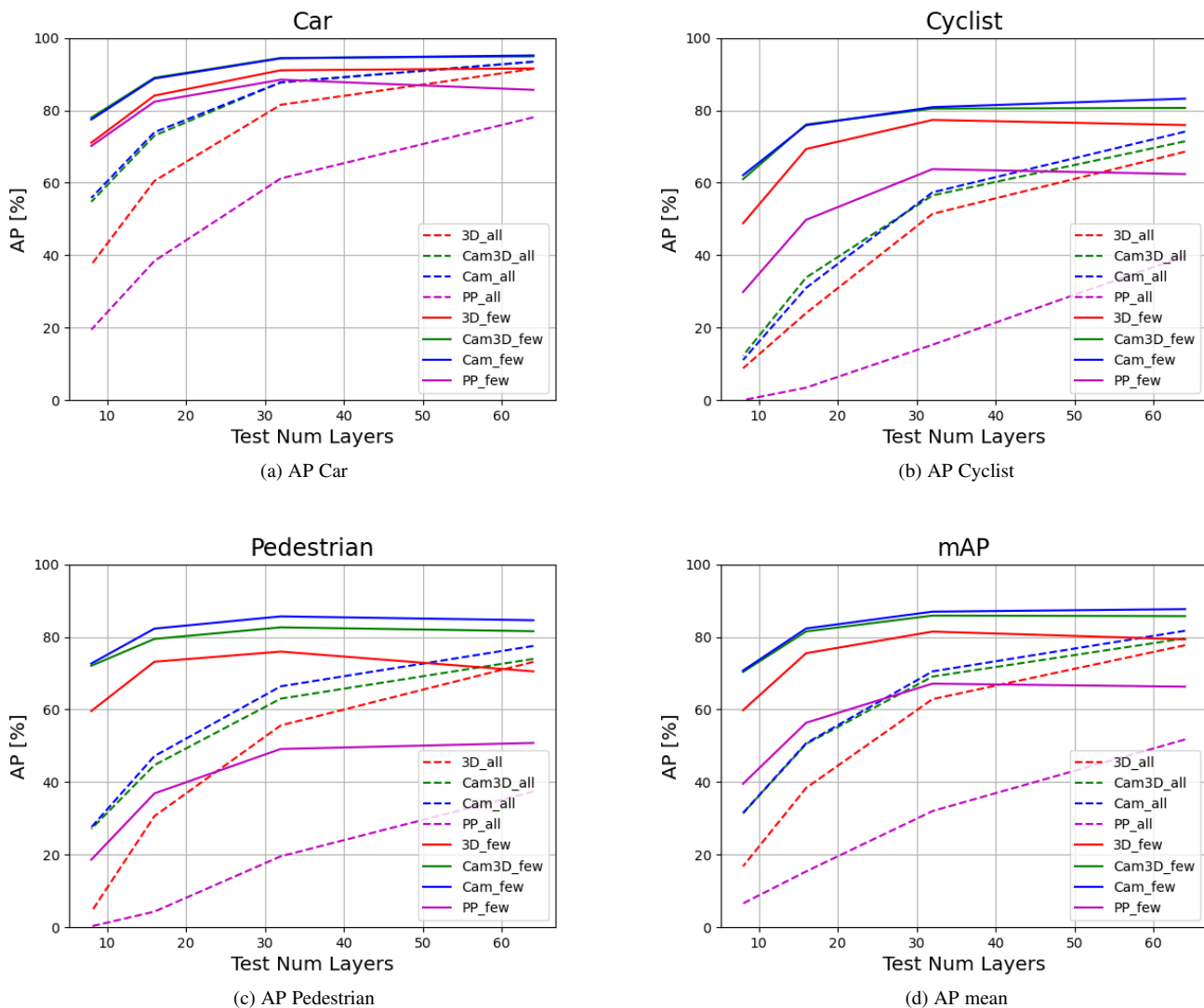


Fig. 6: Evolution of the Average Precision (IoU 0.5) depending on the number of layers in point clouds.

TABLE 4: Average Precision (IoU 0.5) on KITTI Validation set.

Input	Testing number layers	Car	Pedestrian	Cyclist	mAP
<i>PP_all</i>	64	78.06	37.39	39.82	51.75
<i>PP_few</i>		85.65	50.79	62.40	66.28
<i>3D_all</i>		91.46	73.12	68.59	77.72
<i>3D_few</i>		91.57	70.49	75.94	79.34
<i>Cam3D_all</i>		93.42	73.95	71.46	79.61
<i>Cam3D_few</i>		94.89	81.57	80.66	85.71
<i>Cam_all</i>		93.41	77.51	74.13	81.69
<i>Cam_few</i>		<b>95.15</b>	<b>84.58</b>	<b>83.22</b>	<b>87.65</b>
<i>PP_all</i>	8	19.45	0.27	0.0	6.57
<i>PP_few</i>		70.15	18.61	29.82	39.53
<i>3D_all</i>		37.37	4.23	8.78	16.79
<i>3D_few</i>		71.06	59.57	48.8	59.81
<i>Cam3D_all</i>		54.73	27.08	12.29	31.37
<i>Cam3D_few</i>		<b>77.97</b>	72.05	60.99	70.33
<i>Cam_all</i>		55.82	27.54	11.08	31.48
<i>Cam_few</i>		77.45	<b>72.65</b>	<b>62.09</b>	<b>70.73</b>

#### 4.4.1 Contributions of the Training Procedure

Figure 6 illustrates two different types of curve variations depending on the conditions of the training with unchanged (*\_all*) or with modified data (*\_few*). Labeled experiments *\_few* tend to be more resilient to the reduction of input layers than their counterparts labeled *\_all*. For instance, for the PointPillars network (*PP\_*) on the “Car” class (Figure 6a), the difference between the maximum and the minimum measured AP values is 59.06 on *PP\_all* but decreases to 15.5 on *PP\_few*. Moreover, it can be noticed that even if *\_few* experiments are trained on fewer data, they perform better than their equivalent *\_all* on 64 layers LiDAR. The assumption is that for *\_few* experiments, the network learns features that summarize better discriminant aspects than *\_all* experiments as it must identify the targets on fewer data. In that sense, every new point adds information to an already compact but explicit descriptor. These results demonstrate the contribution of our data augmentation procedure on the robustness with respect to variations on the number of layers.

#### 4.4.2 Comparison between 3D Point Cloud Models

In this section, PointPillars and the 3D\_ version of R-AGNO-RPN are compared in order to evaluate the proposed architecture. The focus is on experiments labeled *\_all*. Whatever the number of layers, our network provides better results than PointPillars. However, the difference of performances is more obvious on small targets (Pedestrian, Figure 6c and Cyclist, Figure 6b). The same observations can be noticed on experiments labeled *\_few*. PointPillars manages less but bigger voxels that are processed independently, while 3D\_ generates more but smaller voxels that are directly linked to their respective neighbors through the first convolution. Moreover, contrary to PointPillars that concatenates the features maps from different scales before estimating outputs, the FPN head sub-networks estimate outputs for each feature maps, and then merge them into one output. As a result, each scale can be specialized for a specific type of targets. These results demonstrate the relevancy of our architecture that performs better than PointPillars on the same input data.

#### 4.4.3 Contribution of RGB Images

Table 4 shows that without data augmentation for the training and using the 64 layers at test time, *Cam\_all* and *Cam3D\_all* reach respectively AP of 81.69% and 79.61% while *3D\_all*'s AP is 77.72%. The difference of performance is accentuated when fewer points are available (31.48%, 31.37% and 16.79%, respectively). This drop in performance can be explained as on purely point cloud methods, the result heavily depends on the number of points that are available. Images are regular structures so each pixel of a feature map is highly correlated with its neighbors in the image frame. Even if the point cloud is sparser, only the number of sampled pixels vary, so it is still possible for the RGB feature encoder to tell the difference between a pole and a pedestrian. When these image features are scattered on the BEV map, they already encode information about what could be around the voxel. The input grid, defining the number of voxels and then the number of sampling points, has a fine resolution ( $800 \times 800$ ). In this way, each feature sampled from the RGB map is relocated in space with an acceptable precision. The category of the obstacle may provide a relevant prior for the dimensions of the box. *Cam3D\_all* and *Cam3D\_few* are slightly less efficient than *Cam\_all* and *Cam\_few*. In *Cam\_* experiments, point clouds only intervene for the mapping between the image frame and the BEV frame. However, in *Cam3D\_* experiments the point cloud features are used as inputs for the linear network before the projection on the BEV frame. While point cloud features only encode 3D points located inside each voxel, RGB features already encode high level information that takes account of the neighborhood of the sampling point. Direct fusion at the voxel level may then act as a disturbance for the network because of the difference of information. A latter fusion on intermediate features or a matching between neighborhoods between frames may correct this disturbance.

This experiment shows that RGB images, through the type of information suitable for target identification, can be efficient in BEV object localization if their features can be correctly repositioned in 3D space. Moreover, even on sparse point clouds, the evaluations employing RGB images provide the best results.

#### 4.4.4 Qualitative Results

Figure 7 illustrates some results provided by *Cam\_few* on an unaltered point cloud and a highly trimmed point cloud from

*test* split. Despite the important information loss on the input point cloud, the proposed network is still able to deliver correct proposals with high confidence, even if the scores are generally smaller on reduced data. Due to the reduction of 3D points when layers are removed, some obstacles are no more hit by laser impacts and then are no more detected by the network as no sampling point reaches their representation in the RGB image. In some cases, our network produces more false positives on incomplete data. As the image features are not affected by data reduction, the assumption is that the BEV part still focuses more on the arrangement of the voxels instead of the sampled features. In that sense, a disturbance in the global arrangement may produce unexpected outputs.

### 4.5 Ablation Study

While previous sections focused on the contributions of the RGB image and the training procedure, the following paragraphs introduce the results of the ablation study.

#### 4.5.1 Effects of the Merging Method in FPN Head

In this paragraph, the impact of the merging method in the FPN head is evaluated. Only (*Cam\_few*) is discussed here. Results are detailed in Table 5.

TABLE 5: Comparison between Max and *Softmax* operators for feature maps merging in FPN heads.

Method	Test Number layers	Car	Pedestrian	Cyclist	mAP
<i>Max</i>	64	<b>95.26</b>	34.11	32.2	53.86
<i>Softmax</i>		94.78	<b>83.59</b>	<b>81.86</b>	<b>86.74</b>
<i>Max</i>	8	<b>77.46</b>	31.00	25.1	44.52
<i>Softmax</i>		77.00	<b>71.97</b>	<b>60.98</b>	<b>69.98</b>

On both test conditions, the network operating with a Max operator performs slightly better on Cars. However, its performances drop on Pedestrians and Cyclists. As Cars are the largest objects among the studied targets, they tend to be easier to detect even on low spatial resolution feature maps (such as *out<sub>16</sub>*). Targets labeled with the categories Pedestrians and Cyclists will be more visible on more defined features maps. Features dedicated to small targets are then overwhelmed when using a Max operator. The *Softmax* operator helps to weight the features so smaller objects can still have an impact in the merging process.

#### 4.5.2 Impact of the Input Trimming Patterns

The effects of different patterns are evaluated for the point cloud sub-sampling. For this experiment, the same network (*Cam\_*) is trained through three trimming patterns:

- random uniform sampling (20% – 40% of the points);
- random layer sampling (20% – 40% of the layers).

These two sampling methods are illustrated in Figure 8. The results of the two experiments are illustrated in Table 6.

TABLE 6: Influence of sampling patterns on the performance.

Class	Test Number layers	Car	Pedestrian	Cyclist
Uniform Layers	64	95.12	84.29	80.74
		<b>95.15</b>	<b>84.58</b>	<b>83.22</b>
Uniform Layers	8	67.99	50.20	36.64
		<b>77.45</b>	<b>72.65</b>	<b>62.09</b>

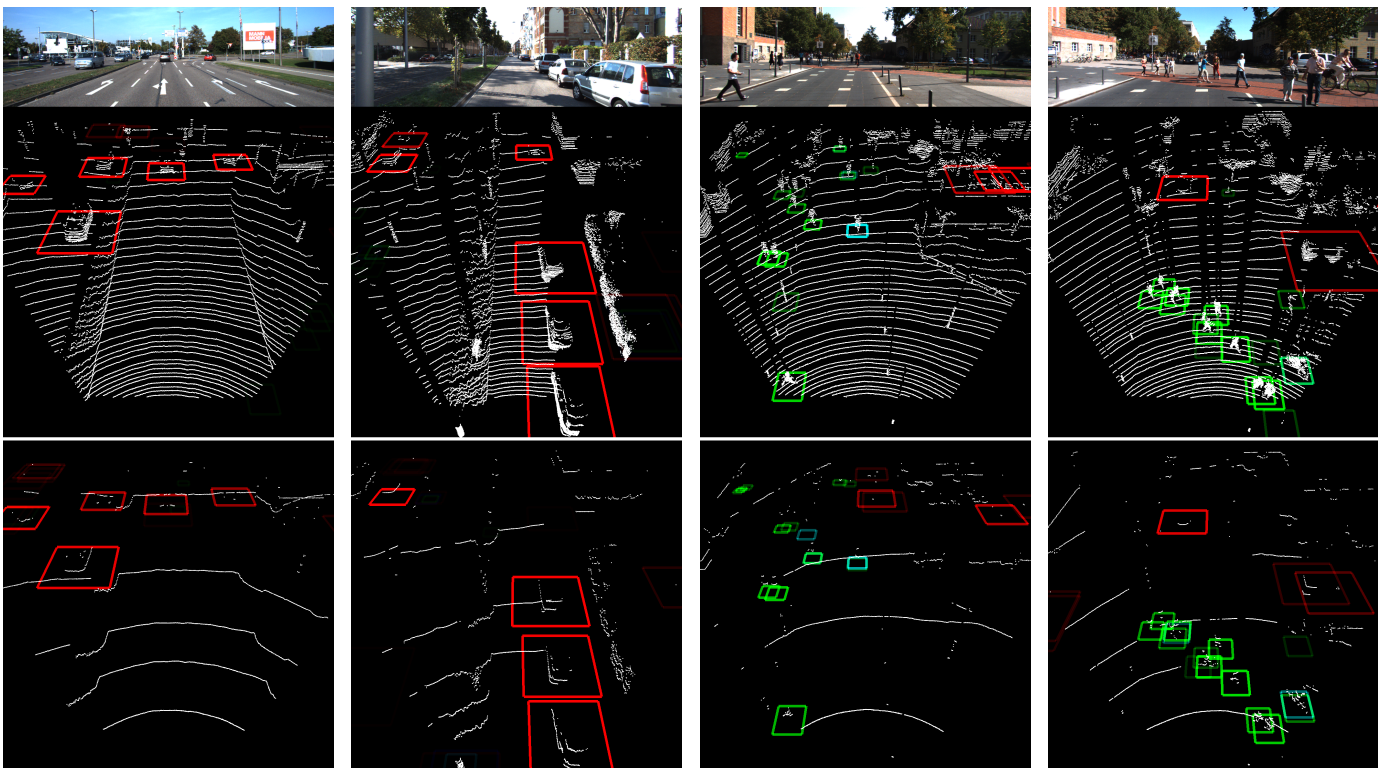


Fig. 7: Qualitative results on KITTI *test* set. The first row contains input images, the second row contains original input point cloud, the third row contains examples with consequent reduction on input point clouds. Colors and transparency of boxes represent the estimated class and the confidence score (red: Car, green: Pedestrian, cyan: Cyclist).

Uniform sub-sampling slightly degrades the performances on 64-layer point clouds. Even if the uniform sub-sampling performs a reduction of the number of points on the training stage, the layered structure of the point cloud delivered by a mechanical LiDAR is no longer respected. This causes the slight drop in performance on unaltered data. Somehow, the training domain and the testing domain do not correspond when using uniform sub-sampling. This difference of domains is highlighted when 8-layer point clouds are used.

#### 4.6 Transfer to nuScenes dataset

This section presents inference results on the nuScenes dataset after pre-training on the KITTI’s one in order to highlight the R-AGNO-RPN’s portability. The main difficulty in this experiment is that two domains are changed, the image domain and the LiDAR domain. A sample of each dataset is illustrated in Figure 9. Images in nuScenes are larger and tend to be duller and are noisier. Moreover, even if data represent urban scenes, the environments captured for KITTI greatly differ from the ones captured for nuScenes. Concerning the point cloud, even if the used LiDAR is a 32-layer sensor, the latitude range is greater than the 64-layer LiDAR used in KITTI. As a result, fewer layers (and then 3D points) are reserved to the ground or objects at eye level.

In order to ensure similar experiment conditions in pre-training with KITTI dataset, only daylight scenes from the Mini version of nuScenes dataset are chosen for the inference. A sample is composed of 6 images and a 360° LiDAR scan. However, in our network, each image is used separately, and for each image, only the corresponding 3D points inside its frustum are kept. In other

words, each initial scene with a 3D LiDAR scan is split into 6 different scenes corresponding to each camera.

Table 7 presents the AP results for the application of several configurations of the proposed network and PointPillars pre-trained on KITTI and applied on nuScenes. Because nuScenes is considered here as test data, the point cloud at inference time is not altered. Scenes in nuScenes tend to be more crowded than the KITTI ones, so the 40 top proposals are extracted.

TABLE 7: nuScenes AP for IoU 0.5.

Method	Car	Pedestrian	Cyclist
<i>PP_all</i>	19.35	0.49	0.04
<i>PP_few</i>	35.22	8.69	1.12
<i>3D_all</i>	18.71	4.07	0.07
<i>3D_few</i>	40.05	12.96	3.08
<i>Cam3D_all</i>	25.75	3.32	0.85
<i>Cam3D_few</i>	53.65	20.95	2.73
<i>Cam_all</i>	21.63	6.19	1.66
<i>Cam_few</i>	<b>57.14</b>	<b>21.38</b>	<b>8.66</b>

As expected, AP values decreased drastically with data that are far from the training distribution. This observation is noticeable on all experiments but especially on PointPillars *PP\_all*. For point cloud-based experiments *PP\_* and *3D\_* the results heavily depend only on input point clouds. Even if the data augmentation improves the final results, pedestrians and cyclists remains the main weaknesses. The different layout of the point cloud layers, due to the different sensor, and the different environments make small targets more difficult to detect. However, *Cam\_* experiments

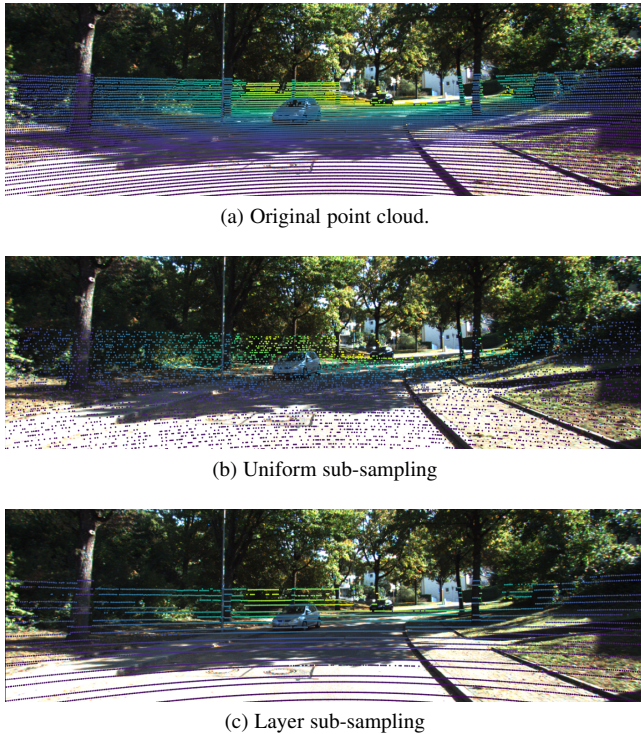


Fig. 8: Comparison between sampling patterns.

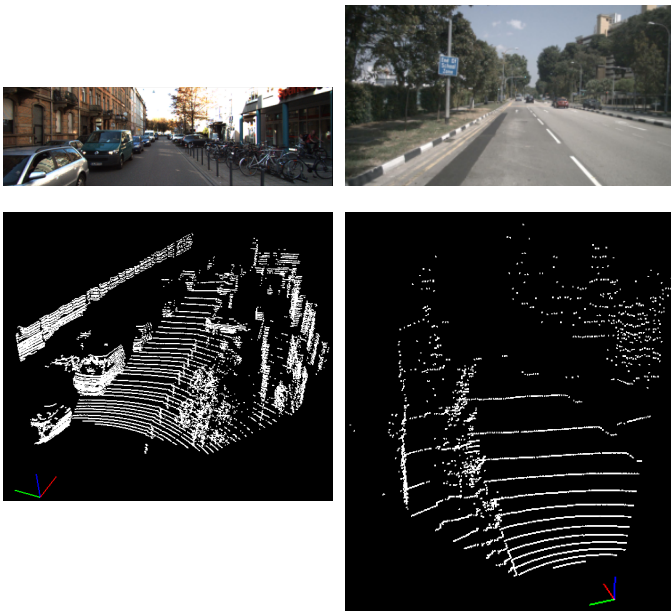


Fig. 9: Comparison between KITTI data (left) and nuScenes data (right).

resist better to this change of context. Generally, the targets keep the same overall aspect, even when captured with different camera sensors with same operation mode (no fish-eye for example) and on the same lighting conditions. Hence, RGB features tend to vary less between datasets allowing to retrieve small targets even if few 3D data is available. Nevertheless, the final results are still affected by the layout of the voxels in the BEV map that depends on the input point cloud.

Furthermore, all the previous findings are still valid in the

nuScenes case: the experiments labeled *\_few* perform better than the ones trained on unaltered data. In fact, by altering the point cloud topology during the training by means of the data augmentation procedure proposed in this paper, the network does not focus on a specific type of layout but better adapt to variations in input data. In that case, the change of LiDAR sensor between KITTI and nuScenes datasets at inference time is the main cause of data variation.

Concerning Cyclist class, as the number of labels in the dataset is minimal, each missed target causes an important drop in AP scores. Moreover, on each data type, Cyclist class may be badly estimated. nuScenes point clouds allocate fewer points to objects close to the ground, thus it is more difficult to identify a bicycle of a bike. On RGB images, depending on its apparent pose, the target can be easily confused with a pedestrian. However, this kind of error will be considered as a false positive on the Pedestrian class and a false negative on Cyclist class, causing in the end an important drop in performance.

Figure 10 illustrates some visual results given by *Cam\_few*. It can be noticed that globally, the proposals cover most of the ground truth boxes. The developed method aims region proposal but not refined box detection. In that way, we displayed in the third line the 40 main proposals. Overall, the provided regions of interest follow the arrangement of the ground truths (second line). However, the fourth line shows that the confidence scores on the proposals are often not well estimated causing the drop in AP. Even if the global aspect of the targets is recognizable, many parameters can cause the confidence score to decrease on the new dataset, for example car models never seen in the KITTI dataset, the contrast between the foreground targets and the background, and even the arrangement of voxels in the BEV map.

This experiment illustrates that even without additional training, our network resists well to change of data domains. The RGB-based network reacts better than the tested point-cloud based methods because of the smaller variations in the input data, images remaining regular grids of pixels and convolutions allowing the application of the same operators that are independent of the camera sensor.

## 5 CONCLUSION

This paper proposes R-AGNO-RPN, a Region Proposal Network that takes advantage of fusion data of Camera images and LiDAR point cloud to deliver accurate axis-aligned bounding boxes, even if the 3D point cloud is sparser and sparser. Feature maps from 2D images are sampled and then scattered on a Bird's Eye View map thanks to the input point cloud. This fusion of 2D and 3D information is then used to estimate the category, the location and the dimensions of regions of interest that encompass possible obstacles. Moreover, we introduced a layer-based data augmentation technique in order to enforce the RGB network to learn more discriminating features at the first blocks to improve the final performance. Our network is compared to a state-of-the-art method, PointPillars, to illustrate its ability to provide accurate results on high and low resolution LiDARs. Experiments involving only point cloud resolution show that the proposed network is able to deliver accurate predictions even if the input point cloud contains few layers. The performances on 64 layers is also improved thanks to the training procedure that forces each pixel to become more informative on its own instead of relying only on its neighborhood. Finally, the experiments on the

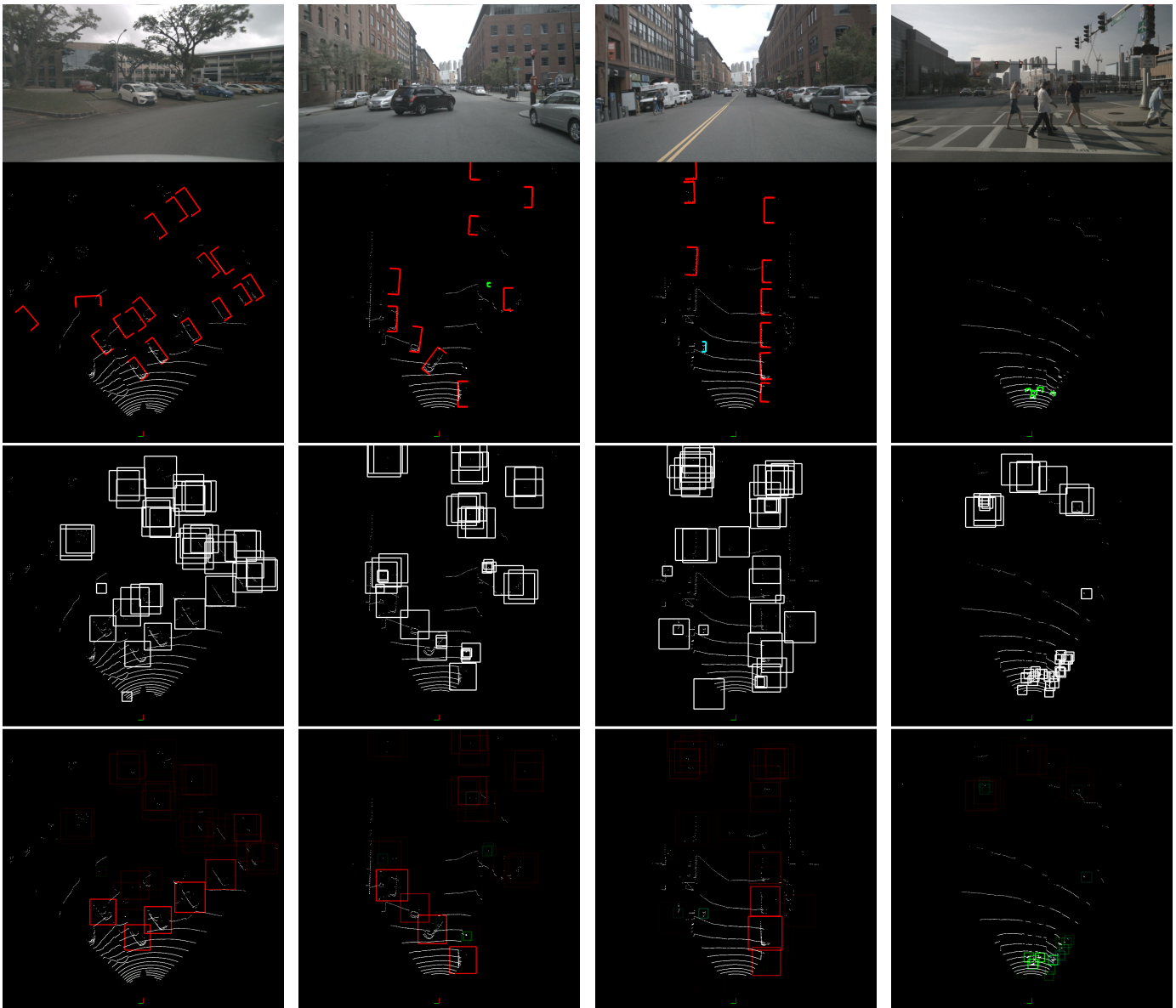


Fig. 10: Qualitative results on nuScenes. The first row contains input camera images. The second one indicates the labels (red: Car, green: Pedestrian, cyan: Cyclist). The third row exposes the 40 top proposals without the score delivered by the network nor the estimated class. The fourth row illustrates the proposals with their estimated class and score through the box color and transparency.

nuScenes dataset exposed promising results on the application of the proposed network on data issued from different sensors (LiDAR and Camera) and recorded on different environments. In fact, despite being only trained on the KITTI dataset, the network is able to locate the potential targets even with the different sensor data existing in the nuScenes dataset. Since the presented system only focuses on region proposition, future work may concern the addition of the second stage to accurately regress the bounding boxes such as precise orientation and the refined dimension and the domain adaptation for better portability on various urban data.

## ACKNOWLEDGMENTS

This work has been sponsored by Sherpa Engineering and ANRT (Association Nationale de la Recherche et de la Technologie). This work has been sponsored also by the French government

research Program Investissements d’Avenir through the RobotEx Equipment of Excellence (ANR-10-EQPX-44) and the IMobS3 Laboratory of Excellence (ANR-10-LABX-16-01), by the European Union through the program Regional competitiveness and employment 2014-2020 (FEDER - AURA region) and by the AURA region. We are grateful to the Mésocentre Clermont Auvergne University and/or AuBi platform for providing help and/or computing and/or storage resources.

## REFERENCES

- [1] Y. Yan, Y. Mao, and B. Li, “SECOND: Sparsely Embedded Convolutional Detection,” *Sensors*, vol. 18, no. 10, 2018. [Online]. Available: <https://www.mdpi.com/1424-8220/18/10/3337>
- [2] C. R. Qi, H. Su, K. Mo, and L. J. Guibas, “PointNet: Deep Learning on Point Sets for 3D Classification and Segmentation,” in *Proceedings of the IEEE Conference on Computer Vision and Pattern Recognition (CVPR)*, 2017, pp. 652–660.

- [3] C. R. Qi, L. Yi, H. Su, and L. J. Guibas, "PointNet++: Deep Hierarchical Feature Learning on Point Sets in a Metric Space," in *Advances in Neural Information Processing Systems*, 2017, pp. 5099–5108.
- [4] S. Shi, X. Wang, and H. Li, "PointRCNN: 3D Object Proposal Generation and Detection From Point Cloud," in *The IEEE Conference on Computer Vision and Pattern Recognition (CVPR)*, June 2019.
- [5] Y. Chen, S. Liu, X. Shen, and J. Jia, "Fast Point R-CNN," in *The IEEE International Conference on Computer Vision (ICCV)*, October 2019.
- [6] S. Vora, A. H. Lang, B. Helou, and O. Beijbom, "PointPainting: Sequential Fusion for 3D Object Detection," in *IEEE/CVF Conference on Computer Vision and Pattern Recognition (CVPR)*, June 2020.
- [7] C. R. Qi, W. Liu, C. Wu, H. Su, and L. J. Guibas, "Frustum PointNets for 3D Object Detection from RGB-D Data," in *Proceedings of the IEEE Conference on Computer Vision and Pattern Recognition*, 2018, pp. 918–927.
- [8] M. Wang and W. Deng, "Deep visual domain adaptation: A survey," *Neurocomputing*, vol. 312, pp. 135–153, 2018.
- [9] A. Geiger, P. Lenz, C. Stiller, and R. Urtasun, "Vision meets robotics: The KITTI Dataset," *The International Journal of Robotics Research*, vol. 32, no. 11, pp. 1231–1237, 2013.
- [10] H. Caesar, V. Bankiti, A. H. Lang, S. Vora, V. E. Liong, Q. Xu, A. Krishnan, Y. Pan, G. Baldan, and O. Beijbom, "nuScenes: A multimodal dataset for autonomous driving," *arXiv preprint arXiv:1903.11027*, 2019.
- [11] T. Roddick, A. Kendall, and R. Cipolla, "Orthographic Feature Transform for Monocular 3D Object Detection," *arXiv preprint arXiv:1811.08188*, 2018.
- [12] S. Shrivastava and P. Chakravarty, "CubifAE-3D: Monocular Camera Space Cubification on Autonomous Vehicles for Auto-Encoder based 3D Object Detection," *arXiv preprint arXiv:2006.04080*, 2020.
- [13] G. Brazil and X. Liu, "M3D-RPN: Monocular 3D Region Proposal Network for Object Detection," in *Proceeding of International Conference on Computer Vision*, Seoul, South Korea, October 2019, pp. 9287–9296.
- [14] A. Simonelli, S. R. Buló, L. Porzi, M. Lopez-Antequera, and P. Kotschieder, "Disentangling Monocular 3D Object Detection," in *Proceedings of the IEEE/CVF International Conference on Computer Vision (ICCV)*, October 2019.
- [15] J. Beltran, C. Guindel, F. M. Moreno, D. Cruzado, F. Garcia, and A. De La Escalera, "BirdNet: a 3D Object Detection Framework from LiDAR information," in *21st International Conference on Intelligent Transportation Systems (ITSC)*. IEEE, 2018, pp. 3517–3523.
- [16] M. Simon, S. Milz, K. Amende, and H.-M. Gross, "Complex-YOLO: An Euler-Region-Proposal for Real-Time 3D Object Detection on Point Clouds," in *Computer Vision – ECCV 2018 Workshops*, L. Leal-Taixé and S. Roth, Eds. Cham: Springer International Publishing, 2019, pp. 197–209.
- [17] Y. Zhou and O. Tuzel, "Voxelnet: End-to-end learning for point cloud based 3d object detection," in *Proceedings of the IEEE Conference on Computer Vision and Pattern Recognition*, 2018, pp. 4490–4499.
- [18] A. H. Lang, S. Vora, H. Caesar, L. Zhou, J. Yang, and O. Beijbom, "PointPillars: Fast Encoders for Object Detection From Point Clouds," in *The IEEE Conference on Computer Vision and Pattern Recognition (CVPR)*, June 2019.
- [19] Q. Chen, L. Sun, Z. Wang, K. Jia, and A. Yuille, "Object as Hotspots: An Anchor-Free 3D Object Detection Approach via Firing of Hotspots," *arXiv preprint arXiv:1912.12791*, 2019.
- [20] T. Yin, X. Zhou, and P. Krährenbühl, "Center-based 3D Object Detection and Tracking," *arXiv:2006.11275*, 2020.
- [21] S. Shi, C. Guo, L. Jiang, Z. Wang, J. Shi, X. Wang, and H. Li, "PV-RCNN: Point-Voxel Feature Set Abstraction for 3D Object Detection," in *Proceedings of the IEEE/CVF Conference on Computer Vision and Pattern Recognition*, June 2020, pp. 10 529–10 538.
- [22] S. Shi, Z. Wang, X. Wang, and H. Li, "Part-A<sup>2</sup> Net: 3D Part-Aware and Aggregation Neural Network for Object Detection from Point Cloud," *arXiv preprint arXiv:1907.03670*, 2019.
- [23] X. Chen, H. Ma, J. Wan, B. Li, and T. Xia, "Multi-View 3D Object Detection Network for Autonomous Driving," in *Proceedings of the IEEE Conference on Computer Vision and Pattern Recognition*, 2017, pp. 1907–1915.
- [24] J. Ku, M. Mozifian, J. Lee, A. Harakeh, and S. L. Waslander, "Joint 3D Proposal Generation and Object Detection from View Aggregation," in *IEEE/RSJ International Conference on Intelligent Robots and Systems (IROS)*. IEEE, 2018, pp. 1–8.
- [25] D. Xu, D. Anguelov, and A. Jain, "PointFusion: Deep Sensor Fusion for 3D Bounding Box Estimation," in *Proceedings of the IEEE Conference on Computer Vision and Pattern Recognition*, 2018, pp. 244–253.
- [26] M. Liang, B. Yang, S. Wang, and R. Urtasun, "Deep Continuous Fusion for Multi-Sensor 3D Object Detection," in *Proceedings of the European Conference on Computer Vision (ECCV)*, 2018, pp. 641–656.
- [27] Z. Yang, Y. Sun, S. Liu, X. Shen, and J. Jia, "IPOD: Intensive Point-based Object Detector for Point Cloud," *arXiv preprint arXiv:1812.05276*, 2018.
- [28] Z. Wang and K. Jia, "Frustum ConvNet: Sliding Frustums to Aggregate Local Point-Wise Features for Amodal 3D Object Detection," in *IEEE/RSJ International Conference on Intelligent Robots and Systems (IROS)*. IEEE, 2019, pp. 1742–1749.
- [29] V. A. Sindagi, Y. Zhou, and O. Tuzel, "MVX-Net: Multimodal voxelnet for 3D object detection," in *International Conference on Robotics and Automation (ICRA)*. IEEE, 2019, pp. 7276–7282.
- [30] M. Liang, B. Yang, Y. Chen, R. Hu, and R. Urtasun, "Multi-task multi-sensor fusion for 3d object detection," in *Proceedings of the IEEE Conference on Computer Vision and Pattern Recognition*, 2019, pp. 7345–7353.
- [31] S. Ren, K. He, R. Girshick, and J. Sun, "Faster R-CNN: Towards Real-Time Object Detection with Region Proposal Networks," *IEEE Transactions on Pattern Analysis and Machine Intelligence*, vol. 39, no. 6, pp. 1137–1149, 2017.
- [32] J. Redmon, S. Divvala, R. Girshick, and A. Farhadi, "You Only Look Once: Unified, Real-Time Object Detection," in *Proceedings of the IEEE Conference on Computer Vision and Pattern Recognition*, 2016, pp. 779–788.
- [33] J. Redmon and A. Farhadi, "YOLOv3: An Incremental Improvement," *arXiv preprint arXiv:1804.02767*, 2018.
- [34] B. Graham and L. van der Maaten, "Submanifold Sparse Convolutional Networks," *arXiv preprint arXiv:1706.01307*, 2017.
- [35] H. Kuang, B. Wang, J. An, M. Zhang, and Z. Zhang, "Voxel-FPN: Multi-Scale Voxel Feature Aggregation for 3D Object Detection from LiDAR Point Clouds," *Sensors*, vol. 20, no. 3, 2020. [Online]. Available: <https://www.mdpi.com/1424-8220/20/3/704>
- [36] T.-Y. Lin, P. Dollár, R. Girshick, K. He, B. Hariharan, and S. Belongie, "Feature Pyramid Networks for Object Detection," in *Proceedings of the IEEE Conference on Computer Vision and Pattern Recognition (CVPR)*, 2017, pp. 2117–2125.
- [37] X. Zhou, D. Dollár, P. Krährenbühl, "Objects as points," *arXiv preprint arXiv:1904.07850*, 2019.
- [38] H. Law and J. Deng, "Cornernet: Detecting objects as paired keypoints," in *Proceedings of the European Conference on Computer Vision (ECCV)*, 2018, pp. 734–750.
- [39] J. Lambert, A. Carballo, A. M. Cano, P. Narksri, D. Wong, E. Takeuchi, and K. Takeda, "Performance Analysis of 10 Models of 3D LiDARs for Automated Driving," *IEEE Access*, vol. 8, pp. 131 699–131 722, 2020.
- [40] F. Piewak, P. Pinggera, and M. Zöllner, "Analyzing the Cross-Sensor Portability of Neural Network Architectures for LiDAR-based Semantic Labeling," in *IEEE Intelligent Transportation Systems Conference (ITSC)*. IEEE, 2019, pp. 3419–3426.
- [41] Z. Wu, S. Song, A. Khosla, F. Yu, L. Zhang, X. Tang, and J. Xiao, "3D ShapeNets: A Deep Representation for Volumetric Shapes," in *Proceedings of the IEEE Conference on Computer Vision and Pattern Recognition (CVPR)*, 2015, pp. 1912–1920.
- [42] I. Achituve, H. Maron, and G. Chechik, "Self-Supervised Learning for Domain Adaptation on Point-Clouds," *arXiv preprint arXiv:2003.12641*, 2020.
- [43] C. Qin, H. You, L. Wang, C.-C. J. Kuo, and Y. Fu, "PointDAN: A Multi-Scale 3D Domain Adaption Network for Point Cloud Representation," in *Advances in Neural Information Processing Systems*, 2019, pp. 7192–7203.
- [44] B. Wu, X. Zhou, S. Zhao, X. Yue, and K. Keutzer, "SqueezeSegv2: Improved model structure and unsupervised domain adaptation for road-object segmentation from a LiDAR point cloud," in *International Conference on Robotics and Automation (ICRA)*. IEEE, 2019, pp. 4376–4382.
- [45] L. Yi, B. Gong, and T. Funkhouser, "Complete & Label: A Domain Adaptation Approach to Semantic Segmentation of LiDAR Point Clouds," *arXiv preprint arXiv:2007.08488*, 2020.
- [46] P. Biber and W. Straßer, "The Normal Distributions Transform: A New Approach to Laser Scan Matching," in *Proceedings 2003 IEEE/RSJ International Conference on Intelligent Robots and Systems (IROS)*, vol. 3. IEEE, 2003, pp. 2743–2748.